

On the carbonation of brucite: Effects of Mg-acetate on the precipitation of hydrated magnesium carbonates in aqueous environment

Hoang Nguyen^{a,*}, Hellen Santos^a, Harisankar Sreenivasan^a, Wolfgang Kunther^b,
Valter Carvelli^c, Mirja Illikainen^a, Paivo Kinnunen^a

^a Fibre and Particle Engineering Research Unit, University of Oulu, Pentti Kaiteran katu 1, 90014 Oulu, Finland

^b Department of Civil Engineering, Technical University of Denmark, 2800 Kgs. Lyngby, Denmark

^c Department A.B.C., Politecnico di Milano, Piazza Leonardo Da Vinci 32, 20133 Milan, Italy

ARTICLE INFO

Keywords:

Carbonation (C)
Kinetics (A)
MgO (D)
Organic acid (D)
Thermodynamic calculations (B)
Hydrated magnesium carbonates

ABSTRACT

The role of organic ligands on the formation of hydrated magnesium carbonates (HMCs) has been remaining unclear. This work reports insights into the effects of Mg-acetate on the carbonation of brucite including the kinetics of reaction, the precipitation of different HMCs, and reaction mechanisms. We found that the organic ligand increases the kinetics of brucite's carbonation and alter the formation and conversion of HMCs. A relatively unknown phase (i.e., giorgiosite) precipitates in the presence of Mg-acetate with nanowire morphology. With the presence of acetate ligand, nucleation sites formed after the breakdown of Mg-acetate complexes and be replaced by the Mg-CO₃ bonds. These sites act as a sink for Mg²⁺ to grow crystals and prevent the passivation layer of HMCs on brucite's surface. Findings reported here can enable an approach to steer pore solution chemistry in the HMC-based binder for better reaction degree, durability, and mechanical properties.

1. Introduction

Cement is an essential material in human history. It is the second most used material on Earth after water and the largest manufactured product by mass. The modern cement—Portland cement—is an excellent material from many perspectives: it has very low cost of production, yet very high performance and durability in a wide range of applications, and it can be produced from local material in most locations. However, Portland cement is a Ca-based binder which hence demands a major source of calcium derived mainly from limestone (CaCO₃). The CO₂ emission of Portland cement manufacturing has reached 866 kg/t [1] in which there are two main sources of CO₂ emission: decomposition limestone and burning fuel for the kilns used [2,3]. Therefore, this industry is responsible for 5–8% total anthropogenic carbon emission, being the second largest industrial CO₂ emitter after steel industry [3]. The consumption and demand for cement will keep increasing to adapt to the rise in human population, and is expected to reach ca. 6 billion tons per annum in 2050 [2]. Hence, the research community has been actively seeking for solutions to mitigate the carbon footprint of this industry.

There are several pathways to reduce the carbon footprint of the

cement industry. The use of supplementary cementitious materials, to reduce the clinker factor, has proved its potential and technical feasibility for decades. This approach will remain as a main route to substitute Portland cement clinker and play a major role in reducing the CO₂ emission of this industry [2,4]. On the other hand, alternative binders attract high attention and several binding systems have been investigated and developed. Since modern binders are based on calcium silicates and aluminates to produce binding properties in which C-S-H, AFt, AFm all require Ca to form [5,6]; this leads to the need of burning limestone as a source of Ca for cement clinkers. To reach the concept of carbon neutrality or a negative carbon footprint, non-Ca-based binders are of increasing interest. Mg-based cement is one of the most promising alternatives that have favorable characteristics [7].

Mg-based cements exhibit unique properties yet high potential for a major binding system. While the amount of CO₂ resulting from MgO production from MgCO₃ is massive (1.5 kg CO₂ per kg MgO produced) compared to the amount of CO₂ resulting from CaCO₃ calcination (ca. 0.786 kg CO₂ per kg of CaO), there is potential for cuts in emission due to Earth's mineralogy [7,8]. While Ca is present predominantly in carbonates, MgO can be extracted from Mg-Si rocks (e.g., forsterite Mg₂SiO₄), which are abundant on Earth and the widely available in different places

* Corresponding author.

E-mail address: hoang.nguyen@oulu.fi (H. Nguyen).

<https://doi.org/10.1016/j.cemconres.2021.106696>

Received 26 June 2021; Received in revised form 7 October 2021; Accepted 17 December 2021

0008-8846/© 2021 The Author(s). Published by Elsevier Ltd. This is an open access article under the CC BY-NC-ND license

(<http://creativecommons.org/licenses/by-nc-nd/4.0/>).

in the world. This direction offers high potential to produce MgO from the decomposition of Mg-rich mineral such as forsterite and serpentine [9]. In addition, if the Mg-based cements are made from carbonation process, the net CO₂ emission of this system can be ca. 73% lower than that of Portland cement [8]. This also leads to a high potential of carbon-negative cements from the carbonation of Mg to produce cementitious binders, in which MgO source comes from Mg—Si minerals.

Many studies have focused on the development of Mg-based cements. M—S—H cement originating from reactive MgO and silica fume (often called low-pH cement) [10,11] is a promising candidate, since it shows binding properties as reported recently in the literature [12]. On the other hand, binders based on hydrated magnesium carbonates (HMCs) have gained attention particularly for its ability to capture carbon. Dung et al. [13–16] have studied the formation and performance of this system starting from reactive MgO and carbonate at ambient pressure with various CO₂ concentration and duration. Kuenzel et al. [17] in 2018 and Winnefeld et al. [18] investigated the hydration mechanism of MgO-hydromagnesite blends and verified several hypotheses (i.e., the role of NaHCO₃ and HMC seeds in the binder) which potentially affect the hydration and formation of phases in MgO-based binders. Since reactive MgO is the most common precursor (i.e., light-burned MgO), brucite [Mg(OH)₂] is formed as an important intermediate hydrate prior to its carbonation to form HMCs. Hence, insights into the carbonation of brucite and formation of HMC are key information for the development of Mg-based binder that may be used for structural components.

Together with valuable understanding, the literature raised new research questions, which are opened up based on findings from previous works reported in Ref. [14,15,18,19] for Mg-based binders. Winnefeld et al. [18] confirmed negative response toward their 2 hypotheses about the role of artinite in seeding HMC precipitation and NaHCO₃ as an accelerator of the MgO-hydromagnesite blends. However, the presence of hydromagnesite seems to play an important role in the reaction kinetics since in their presence the system formed different hydrates, the identity of which remains unknown. Dung et al. [19] used Mg-acetate as an hydrating agent in their reactive Mg-based cement produced from light-burned MgO. The presence of Mg-acetate was reported to facilitate the formation of HMC via an increase in the amount of brucite formed. This was used to explain higher carbonation degrees, denser microstructure, and consequently higher mechanical properties (by 40%). However, the mechanism of these phenomena and the interaction between brucite and Mg-acetate, which introduce acetate as an organic ligand into the system, remain unclear. Notably, the literature of aqueous carbonation for brucite has been extending in recent years due to the urgent need for a carbon sink [20–23].

In this study, we aim to obtain insights into the carbonation of brucite in an aqueous environment with the presence of acetate as an organic ligand. This will shed light on several remaining open questions:

- What is the role of Mg-acetate in the carbonation process toward the formation of HMC?
- Whether the ligand alters the kinetics of carbonation and/or hydration of the system?; and
- Which HMC is favorable in terms of mechanical properties?

To this end, we performed the carbonation of brucite in aqueous environment where Mg-acetate is used as an organic admixture at different dosages. The findings reported here will contribute to the progress and advances in developing carbon-negative cements from Mg-based binders with some fundamental understanding of the precipitation of HMCs.

2. Materials and methods

2.1. Precursors

Brucite (VWR Finland, purity 95.0–100.5%, CAS number: 1309-42-8) was used as received without further treatment. The median particle size of brucite is ca. 8 μm. Reagent-grade sodium bicarbonate (NaHCO₃; Sigma-Aldrich, purity ≥99.5%, CAS number: 144-55-8) is the carbonate source in this study. Mg-acetate tetrahydrate [(CH₃COO)₂Mg·4H₂O; Sigma-Aldrich, purity ≥99%, CAS number: 16674-78-5] is the source of acetate ligand.

2.2. Carbonation of brucite in aqueous environment

Mg-acetate solutions of different concentrations were prepared by dissolving Mg-acetate tetrahydrate in deionized water; the water was bubbled with N₂ gas for 15 min to remove dissolved carbonate prior to its use. Three different concentrations of Mg-acetate solutions were prepared: 0.01, 0.1, and 1 M.

Table 1 shows the mix recipes of suspensions with and without Mg-acetate. Brucite and NaHCO₃ were dry mixed together in a fixed molar ratio of 1. The liquid-to-solid ratio was set to 7, which provides sufficient water for the dissolution and carbonation of brucite. The suspension was sealed in a plastic container and stirred by a magnetic capsule at 150–200 rpm for 30 min. Samples were collected after 1, 7, and 28 days by vacuum filtration with a 10-μm filter, during which the precipitate was washed twice by isopropanol to remove leftover water. Solid samples were then dried at 50 °C for 1 day and kept in plastic containers prior to further analyses. The pH of suspensions was measured with a Hach pH electrode (code: PHC28101) in situ for the first 24 h and ex situ after 7 and 28 days.

2.3. Dissolution of brucite in Mg-acetate solution

To shed further light on the role of the acetate ligand on the carbonation of brucite, brucite was dissolved in 1 M Mg-acetate solution and compared to a sample dissolved in deionized water. The mix recipes were kept the same as in Table 1 without adding NaHCO₃. Solutions were bubbled with N₂ gas for ca. 15 min to reduce any carbon contamination prior to their use. The experiments were performed in a glove box filled with N₂ gas, while all suspensions were sealed in plastic containers and continuously shaken with ca. 200 motions per min. Samples were filtrated and collect after 1, 7, and 28 days in which both solids and solutions were characterize afterward. The solids followed the same treatment and procedure as for precipitates in Section 2.2, whereas the suspensions were measured pH and their solutions were acidified by HNO₃ 6.5% (acid-to-liquid ratio = 3) to further measurement.

2.4. Material characterization

2.4.1. Q-XRD

XRD analysis was performed on powdered samples with a Pan-Analytical apparatus (model X'pert³ MRD), employing Cu-Kα radiation (Kα₁ = 1.54 Å) using a voltage and current of 40 kV and 45 mA, respectively. The measurements were conducted at a scan rate of 0.0167°/min in the range 5°–70° (2θ) and 0.017°2θ/step. Quantitative

Table 1

The mix recipes of suspension with and without the presence of Mg—Ac.

Mix ID	Brucite (g)	NaHCO ₃ (g)	Water (ml)	Mg-acetate solution (ml)
Plain	2.9	4.2	50	–
With Mg-Ac ^a	–	–	–	50

^a In 3 different concentrations: 0.01, 0.1, and 1 M.

XRD analysis was used to determine the fraction of amorphous phases in the precipitates using ZnO at ca. 10 wt% as an internal standard. Phase identification was done with PDXL V.2 software (Rigaku, Japan) and a PDF-4+ 2020 database.

2.4.2. TGA coupled with mass spectrometry (TG/MS)

TG/MS analyses were done with a Netzsch STA 449F3 (Selb, Germany) for roughly 40–50 mg of powdered sample. Alumina crucibles were used, while the system heats from 40 °C to 1005 °C with a ramp of 5 °C/min in a nitrogen atmosphere with a flow rate of 180 ml/min.

2.4.3. SEM

The morphology of precipitates was observed via SEM micrographs using a Zeiss (Oberkochen, Germany) Ultra Plus field emission scanning electron microscope (FE SEM) instrument at a 15 kV accelerator voltage and a working distance of 8–10 mm using backscattered electron. Secondary electron was used to observe the morphology of samples. Samples were coated with Pt (thickness ca. 70 nm) and cure in a desiccator prior to the analyses.

2.4.4. FTIR

The chemical bonds formed at molecular level in the HMC materials were analyzed with FTIR measurements. The spectra were determined at room temperature in the range of 400–4400 cm⁻¹ using a Bruker Vertex 80 spectrometer (Billerica, MA, the U.S.) equipped with a N₂ cooled MCT detector and DRIFT cell accessory. For each spectrum, a total of 32 interferograms were co-added using 8 cm⁻¹ as resolution.

2.4.5. Isothermal calorimetry

Heat evolution during the carbonation of brucite was observed with isothermal conduction calorimetry (TAM Air, TA Instruments, the U.S.). The temperature was set to 23 °C, in which chamber's temperature was stabilized for 1 day before use. Samples were mixed ex situ in glass ampoules for ca. 5 min prior to inserting into the TAM Air calorimeter. The baseline of equipment was determined before injecting the glass ampoules into it. Reference samples contained deionized water with equivalent liquid volume with the evaluated samples. The heat flow signal was recorded automatically for a total duration of 7 days.

2.4.6. Nano indentation

The samples were prepared following the recipe in Table 1. However, the precipitates were in powdered form and hence challenging to precisely characterize their modulus via nano indentation. Therefore, we reduced the liquid-to-solid ratio in these samples to obtain compact solids. The samples were cast into a low-viscosity epoxy and cured at room temperature until the resin hardened. The samples were then polished with diamond discs of #200–1200 and cloth discs of 3–1 µm at 150 rpm using ethanol as lubricant. Nano indentation was conducted by NanoTest® system (Micro Materials Ltd., the UK), equipped with a diamond Berkovich tip, at a controlled temperature of 26 °C. Loading and unloading rates were set to 0.5 mN/s and 1 mN/s, respectively, in order to reduce the time-dependent effects on the unloading curve. Moreover, a dwell period of 10 s was used at maximum load. A grid of 8 × 8 indentations was performed on each sample, setting 10 mN as maximum force and 25 µm as spacing between adjacent indentations. The latter was adopted to avoid indentation size effect on the modulus measurements. The reduced elastic modulus E_r was obtained from each indentation load-unload curve as

$$E_r = \frac{\sqrt{\pi}}{2\beta\sqrt{A}} S \quad (1)$$

where β is a dimensionless correction factor for indenter tip shape, $\beta = 1.05$ for Berkovich indenter; S is the unloading indentation stiffness; A is the contact area at the maximum indentation depth.

2.5. Thermodynamic modelling

Thermodynamic calculations for the system were conducted in GEMS, developed by Paul Scherrer Institute (Switzerland) [24,25]. The modelling is based on Gibbs free energy minimization method. Cemdata18 database [26] together with default database in GEMS were used for MgO-CO₂-H₂O system at ambient pressure and temperature. Moreover, several additional HMCs were added since GEMS's default databases did not contain these crystals. The thermodynamic properties of these HMCs were collected from Ref. [27–32] as reported in Ref. [18]; the detailed properties, including $\log K^0$, $\Delta_f H^0$, S^0 , C_p^0 , and V_m , can be found in Table 2. Note that the $\log K^0$ values reported in Table 2 were referred to reactions among Mg²⁺, CO₃²⁻, OH⁻ and H₂O in the system using the Nagra/PSI thermodynamic database [33] in GEMS. However, the $\log K^0$ of dypingite were adopted from Ref. [28], while its S^0 and C_p^0 were estimated according to Ref. [34] from the respective values of hydromagnesite and structural water. Furthermore, the thermodynamic database did not contain other HMCs, such as barringtonite (MgCO₃·2H₂O), pokrovskite [Mg₂(CO₃)(OH)₂], giorgiosite [Mg₅(CO₃)₄(OH)₂·5–6H₂O], an unnamed dypingite-like phase [Mg₅(CO₃)₄(OH)₂·8H₂O], protohydromagnesite [Mg₅(CO₃)₄(OH)₂·11H₂O], and shelkovite [Mg₇(CO₃)₅(OH)₄·24H₂O] [35] since their thermodynamic properties are not available in accessible references. Magnesite (MgCO₃) was not considered to precipitate in this system since the phase requires high pressure and temperature to overcome its kinetic hindrances [36].

To introduce Mg-acetate and its complexes in the database and modelling, an acetate ligand (named as *Acetate*) was created as an independent component with the thermodynamic properties shown in Table 3. An acetate ion (*Acetate*⁻) was also created as a dependent component in the database using the thermodynamic data of the acetate ligand. The thermodynamic data of acetate complexes were then added into GEMS's database as shown in Table 4.

3. Results

3.1. Precipitates from carbonated brucite

Fig. 1 shows the precipitates that formed in samples with different dosages of Mg-acetate. Nesquehonite formed first and was the main crystal in all samples after 1 day, while there was a trace of dypingite in the reference sample and samples with 0.01 and 0.1 M Mg-Ac. Brucite was not fully carbonated and remained in all samples. Later, nesquehonite converted to dypingite with only a trace of nesquehonite left in all samples except the mix with the highest dosage of Mg-acetate, where nesquehonite remained stable after 7 days. There was also a trace of giorgiosite [Mg₅(CO₃)₄(OH)₂·5–6H₂O] in this sample. After 1 month, plain samples and samples with low dosages of Mg-acetate contained mainly dypingite and brucite. In contrast, nesquehonite later fully converted to giorgiosite in the sample with 1 M Mg-Ac solution. Interestingly, there was no brucite left in this sample indicating the full carbonation of this phase. In addition, with the absence of brucite, there was a negligible amount of precipitate (only ca. 1.1 g of nesquehonite via thermodynamic estimation) formed during the reaction of 1 M Mg-Ac and NaHCO₃. Note that from this point onward, we focus mainly on the plain material and the mixture containing the highest Mg-acetate concentration (1 M Mg-Ac) to capture the most distinguishable effects of this organic ligand, which is most prominent at high dosages.

Fig. 2 shows the degrees of reaction of brucite in water and 1 M Mg-Ac determined as determined by QXRD. The results indicate a faster brucite carbonation in ligand-containing solutions compared to water. After 1 day of reaction, brucite carbonated by ca. 65% in 1 M Mg-Ac solution, while only 10% of brucite had reacted in water. Furthermore, the ligand seems to promote the carbonation of brucite. After 1 month, brucite reacted completely in Mg-acetate solution, whereas the only 50 wt% of the brucite carbonated in water.

Fig. 3 shows the evolution of pH in samples without and with Mg-

Table 2

Standard thermodynamic properties of various HMCs at 25 °C and 1 bar used in thermodynamic calculation.

Phase	$\log K^0$	$\Delta_f G^0$ [kJ/mol]	$\Delta_f H^0$ [kJ/mol]	S^0 [J/(mol × K)]	C_p^0 [J/(mol × K)]	V_m [cm ³ /mol]
Nesquehonite, MgCO ₃ ·3H ₂ O	−5.34	1724.0	−1977.3	195.6	237.8	74.8
Lansfordite, MgCO ₃ ·5H ₂ O	−5.24	−2197.8	−2574.3	249.5	317.9	103.2
Hydromagnesite, Mg ₅ (CO ₃) ₄ (OH) ₂ ·4H ₂ O	−38.47	−5864.7	−6504.1	541.3	571.3	208.8
Dypingite, Mg ₅ (CO ₃) ₄ (OH) ₂ ·5H ₂ O	−34.94	−6081.7	−6777.4	585.9	611.3	225.9
Artinite, Mg ₂ (CO ₃)(OH) ₂ ·3H ₂ O	−18.67	−2568.6	−2920.6	232.9	296.1	96.9

Table 3

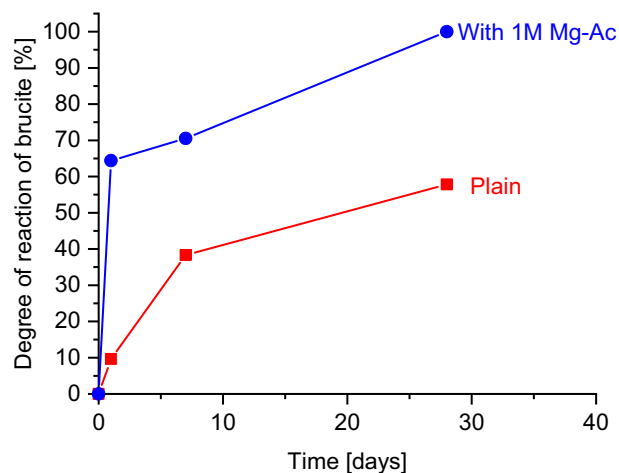
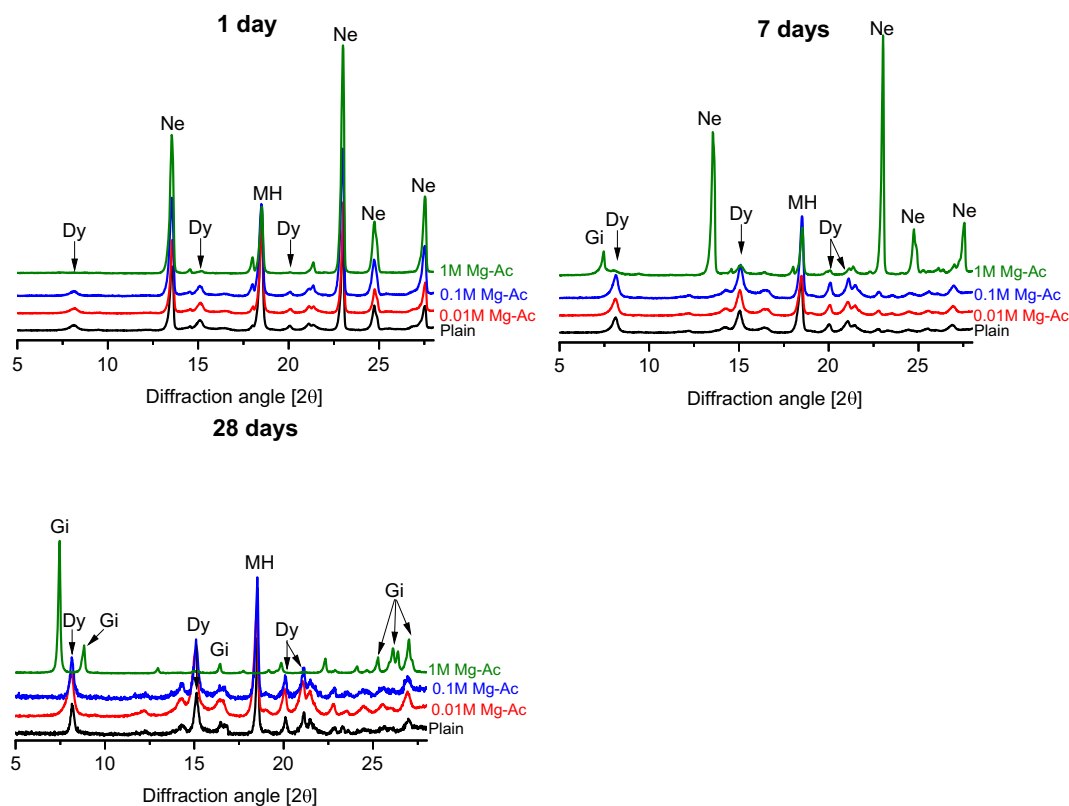
Data for acetate ligand (Ac) calculated as independent component in GEMS.

Ligand	Atomic mass (M_{oi})	Standard-state absolute entropy (S_{oi})	Formula charge ($Valens$)	Standard-state absolute heat capacity (Cp_{oi})	Standard state volume (V_{oi})
Acetate	59.0526	158	−1	123.1	−1.8

Table 4

Thermodynamic data for acetate and its complexes in the system.

Aqueous species	Reaction	$\log K_{so}$	ΔH [kJ/mol]
H(Acetate)	$H^+ + Acetate^- = H(Acetate)$	4.7	0.41
Mg(Acetate)+	$Mg^{2+} + Acetate^- = Mg(Acetate)^+$	1.27	−
Mg(Acetate)2	$2H(Acetate) + Mg^{2+} = Mg(Acetate)2$	211.3	−1206.1
Na(Acetate)	$Na^+ + Acetate^- = Na(Acetate)$	−0.18	12
Na(Acetate) ^{2−}	$Na^+ + H(Acetate) = Na(Acetate)^{2−} + 2H^+$	175.1	−986.2

**Fig. 2.** The degree of reaction of brucite with and without the presence of Mg—Ac dete.**Fig. 1.** The precipitates from the carbonation of brucite with and without the presence of Mg—Ac from 1 to 28 days in aqueous environment. Note that Dy = dypingite, Ne = nesquehonite, Gi = Giorgiosite, and MH = brucite.

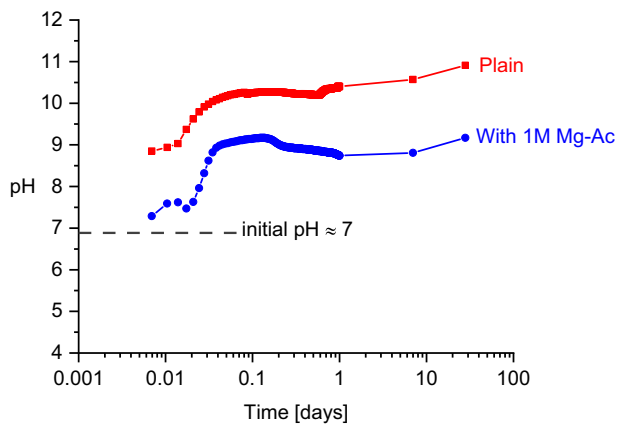


Fig. 3. The pH of suspension samples measured in situ (with an interval of 5 min) for the first day and ex situ after 7 and 28 days.

acetate. The pH in the plain sample raised quickly and reached a pH of ca. 9 after 10 min of reaction. The pH of the Mg acetate free sample remained fairly stable in which its pH was ca. 10–11 after 7 and 28 days, respectively. In contrast, the suspension with 1 M Mg-Ac exhibited lower pH although the pH of the starting solutions (i.e., deionized water and 1 M Mg-Ac solution) was comparable (pH ≈ 7). The pH of the ligand-containing sample was delayed and started to increase after 30 min of reaction and reached pH 9 within an hour. Notably, the pH reduced slightly after 5 h and stabilized around pH 8.5; this is caused by the precipitation of HMCs from the suspension, leading to the reduction of HCO_3^- concentration, similarly to the case of calcite [37].

Fig. 4 shows the FTIR spectra of the precipitates after 1, 7, and 28 days of carbonation with and without the presence of acetate ligand. The magnesium atom in brucite in an octahedral geometry with its hydroxyls ligands, where the hydroxyl ions occupy the C_{3v} sites, which generates a strong IR band at 3698 cm^{-1} due to the antisymmetric O–H stretching vibrations [17,38]. After 1 day of reaction the OH^- stretching vibrations of the water molecules in the crystal structure of nesquehonite are clearly seen through the band at 3560 , 2636 , 2485 , and 2356 cm^{-1} [39–42], which has higher intensity in the ligand-containing sample and thus indicating a higher degree of nesquehonite formation in this sample. After 7 days, these bands are seen only for the 1 M Mg-Ac sample with the addition of a shoulder at 3442 cm^{-1} also assigned to the OH^- stretching mode [41], whereas nesquehonite converted to dypingite in the plain sample. The bands characteristic of dypingite are noticed only for the reference sample. The stretching of the coordinated water in dypingite is seen in the broad band centered at 3400 cm^{-1} which aggregates the characteristic bands at 3447 and 3380 cm^{-1} , being noticed only for the reference sample after 1, 7, and 28 days of reaction, but being more pronounced after 28 days of reaction. The bending of the coordinated water is seen in the band at 1599 cm^{-1} , which is evident only in the IR spectra of the reference samples after 7 and 28 days of reaction. The symmetric stretching of the CO_3^{2-} groups coordinated to dypingite are also noticed only in the IR spectra of the reference samples after 1, 7, and 28 days of reaction through the bands at 1438 and 1380 cm^{-1} , whereas the bending vibrational modes of the carbonate groups is seen only in the IR spectrum of the reference sample after 28 days of reaction in the weak bands at 882 (ν_2) and 755 (ν_4) cm^{-1} . The bending of the Mg–OH groups in dypingite is seen in the weak band at 1008 cm^{-1} in the IR of the reference sample after 28 and 7 days of reaction [43].

As observed from XRD (Fig. 1), giorgiosite is the major HMC in the

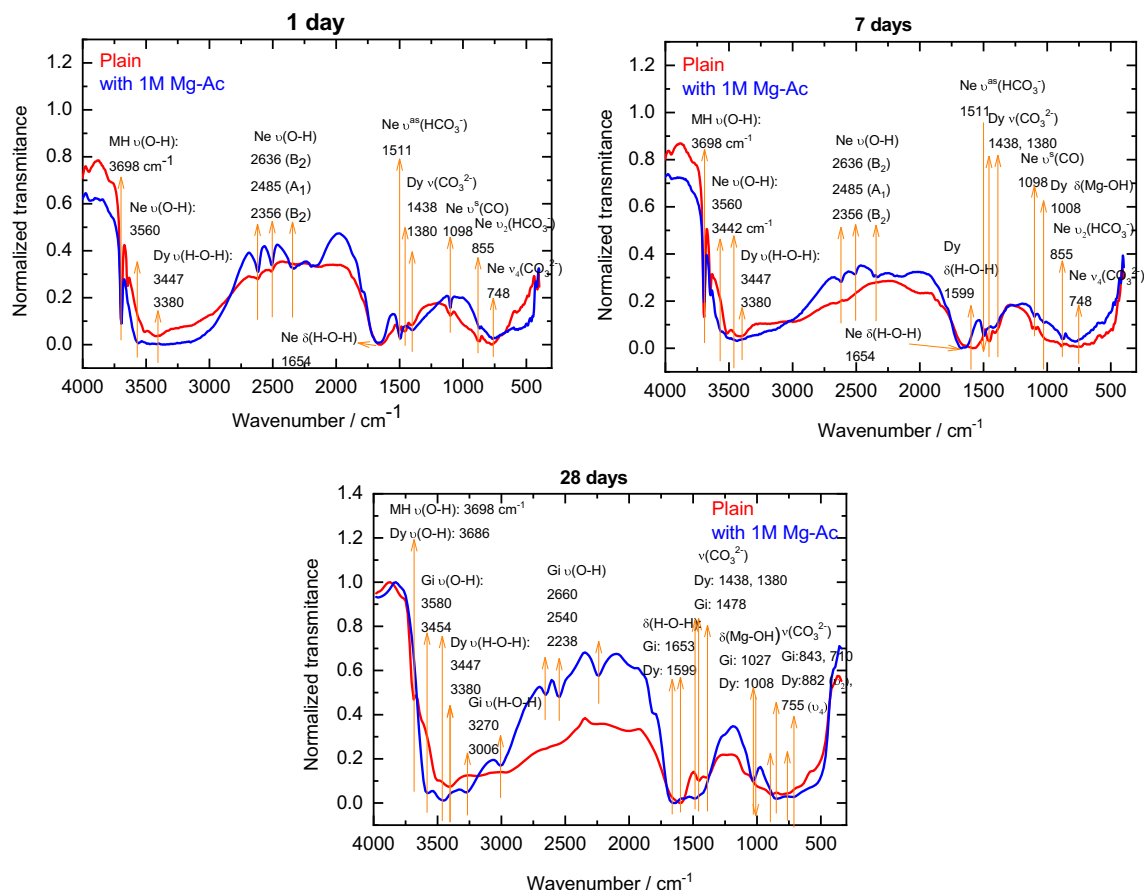


Fig. 4. FTIR spectra of the precipitates after 1–28 days from the carbonation of brucite with and without the presence of Mg–Ac. Note that Dy = dypingite, Ne = nesquehonite, Gi = Giorgiosite, and MH = brucite.

ligand-containing sample after 1 month of reaction. However, the assignment of its IR bands in the FTIR spectra are without reference, since there are no FTIR spectra of giorgiosite published in open literature. Therefore, based on the XRD characterization of the 1 M Mg-Ac sample after 28 days, we assumed that all FTIR bands seen for the same sample are regarded to the vibrational modes of giorgiosite. Fig. 4 and Table 5 shows the observed IR bands for the giorgiosite in the 1 M Mg-Ac sample after 28 days. The same bands are observed at weaker intensity in the IR spectrum of that sample after 7 days of reaction strengthened our arguments for these assignments since giorgiosite was already found in the sample after 7 days.

Fig. 5a shows the thermal decomposition of the precipitates after different ages, while Fig. 5b provides the thermal behaviors of brucite and synthetic nesquehonite as reference phases. The dehydration of HMCs started from ca. 60 °C to 300 °C. Nesquehonite broke down its chemically bound water in 3 steps at 127, 162, and 217 °C (similar to Ref. [44]); this was observed clearly in the ligand-containing sample at 1 day. In contrast, dypingite and/or dypingite-like phases exhibited 2 thermal events before 300 °C: dehydration at ca. 110 °C and dehydroxylation at 205 °C. The plain samples at 28 days show these typical thermal decompositions since the samples contain mainly dypingite, as observed from XRD and FTIR. In addition, the conversion from nesquehonite to dypingite in the plain sample after 1 day also transpired with a slight mass loss at ca. 162 °C. Giorgiosite in the sample with 1 M Mg-Ac had a predominant dehydration at 127 °C, while there was only a slight mass loss caused by dehydroxylation at ca. 300 and 390 °C.

The decarbonation of samples started from ca. 250 °C and last until near 500 °C, while the dehydroxylation of $\text{Mg}(\text{OH})_2$ was also in a similar range from 250 to 400 °C (Fig. 5). In the ligand-containing sample at 1 day, the mass losses at ca. 300 and 380 °C are attributed to nesquehonite's decarbonation, which is lower than reported in Ref. [44,45] and our synthetic nesquehonite (Fig. 5b). In contrast, giorgiosite dehydroxylated at 300 and 400 °C and exhibit the decarbonation also at around 300 °C in the 28-day ligand-containing samples. In the reference sample, thermal events in a range of 300–550 °C were highly overlapped between dehydroxylation and decarbonation of various HMCs and leftover brucite. Notably, these events were distinguishable among plain samples at different ages, indicating the change in phase assemblage as well as hydration stage of dypingite in the precipitates.

Fig. 6 shows the morphology of samples with and without Mg-acetate at different ages. Nesquehonite exhibited its typical needle-like shape [46], in which the conversion to dypingite happened on nesquehonite's surface as seen in the plain sample after 1 day. After 7 and 28 days, the plain sample contained dypingite as the dominant phase; this agrees with the XRD results shown in Fig. 1. In the sample with 1 M Mg-Ac, nesquehonite was the main precipitate from 1 to 7 days of carbonation. Notably, the morphology of nesquehonite in these ligand-containing samples was wider ($17.8 \pm 4.1 \mu\text{m}$) and slightly shorter compared to that of plain sample ($3.7 \pm 1.3 \mu\text{m}$). In addition, some minor HMCs were observed in the sample with acetate ligand, which were likely dypingite and giorgiosite in a minor quantity. However, after a month of reaction, giorgiosite appeared to be the main HMC as the result from the conversion of nesquehonite. Giorgiosite is also needle shaped, but much longer and thinner compared to nesquehonite.

Table 5

IR spectra of giorgiosite identified in the 1 M Mg-Ac sample after 28 days of reaction.

IR bands (cm^{-1})	Assignment
3580; 3454	$\nu(\text{O}-\text{H})$
3270; 3006	$\nu(\text{H}-\text{O}-\text{H})$
2660; 2540; 2238	$\nu(\text{O}-\text{H})$ and $\delta(\text{O}-\text{H})$
1653	$\delta(\text{H}-\text{O}-\text{H})$
1478	$\nu(\text{CO}_3^{2-})$
1027	$\nu(\text{Mg}-\text{O}-\text{H})$
843; 710	$\nu(\text{CO}_3^{2-})$

Fig. 7 shows the heat evolution of the carbonation of brucite with and without acetate ligand. Note that the first heat event observed in both samples was an endothermic reaction from the dissolution of NaHCO_3 , while the main exothermic peak is assigned to the precipitations of HMCs from the carbonation of brucite. The organic ligand retarded the reactions slightly, for which the main peak was shifted by ca. 2 h. In addition, the peak of ligand-containing sample was broader with a slight hump after 3–5 h of reaction in comparison to the plain sample. Generally, the heat evolution of both samples happened relatively quickly in which no clear secondary peak was observed after 1 day. The cumulative heat curves (Fig. 7b) indicate a lower total heat release from the sample with 1 M Mg-Ac whereas the plain sample released ca. 24% more heat in the total heat after 7 days. This can be due to the conversion from nesquehonite to dypingite at very early age in the plain sample.

Fig. 8 shows the distribution of the reduced elastic modulus in precipitates of plain and ligand-containing samples after different ages. The modulus of precipitates in the reference sample ranged from 2 to ca. 30 GPa, while the sample after 7 days attain a smaller range with a modulus of 2–10 GPa. In contrast, the modulus of sample with 1 M Mg-Ac exhibited a gradual change in its elastic modulus after 1 month; the modulus reached ca. 50 GPa and the distribution curve was wider than other early-age samples including the reference. In addition, the distribution of elastic modulus in the ligand-containing sample leaned more toward to higher value over hydration time. The modulus of precipitates in the ligand-containing sample increased slightly after 7 days of age in which the distribution range expanded from max. 20 GPa to max. 30 GPa. In contrast, the plain sample exhibited a narrower distribution in elastic modulus after 1 month of reaction. It worth mentioning that conducting the nanoindentation on the considered mixes has some critical issues related to the possible effect of the intermix pores on the micromechanical properties of the phases [47]. Such effect has been overcome partially by deleting the abnormal indentation test points ($E_r > 400 \text{ GPa}$).

3.2. Dissolution of brucite in Mg-acetate solution

Fig. 9 shows the characteristics of solids collected from suspensions after dissolution tests at different periods. Only brucite was determined via XRD in all samples and there were no carbonated phases seen in these solids. However, the TG/DTG results (Fig. 9b–c) show significant differences in thermal behavior between plain and ligand-containing samples. The reference sample exhibited typical mass loss of brucite in the range of ca. 300–500 °C for its dehydroxylation. In contrast, the brucite in Mg-acetate solution attained distinguishable thermal behavior linking to the sorption of acetate on brucite. The ligand desorption happened at later stage leading to identical DTG curves between plain and ligand-containing samples after 1 month of dissolution. This also transpired via SEM observation shown in Fig. 10. The morphology of brucite in water and Mg-acetate solution after 1 month of dissolution was distinct. The brucite in acetate solution started peeling off its layers with more rounded morphology. Moreover, etch pits clearly presented in the solid. In contrast, the plain sample retained its hexagonal shape of brucite showing limited dissolution of this phase in water.

Fig. 11 shows the FTIR spectra of the brucite after 1, 7, and 28 days of dissolution in water and Mg-acetate solution. In water, brucite had a trace of single asymmetric stretching band between 1478 and 1450 cm^{-1} attributed to carbonate impurities in the brucite as observed previously [17,38]. Moreover, the shoulder near 1650 cm^{-1} was the bending vibration of water [17]. In contrast, ligand-containing samples proved the absorption of acetate on brucite at 1 and 7 days, while the desorption happened at later stage as captured after 1 month. Brucite in acetate solution exhibited C–O asymmetric stretch (1581 cm^{-1}), CH_3 asymmetric bend (1452 cm^{-1}), and in-plane CH_3 rocking (1022 cm^{-1}), which are typical for acetate ligand [48]. However, after 1 month of dissolution in the ligand-containing environment, the spectrum of

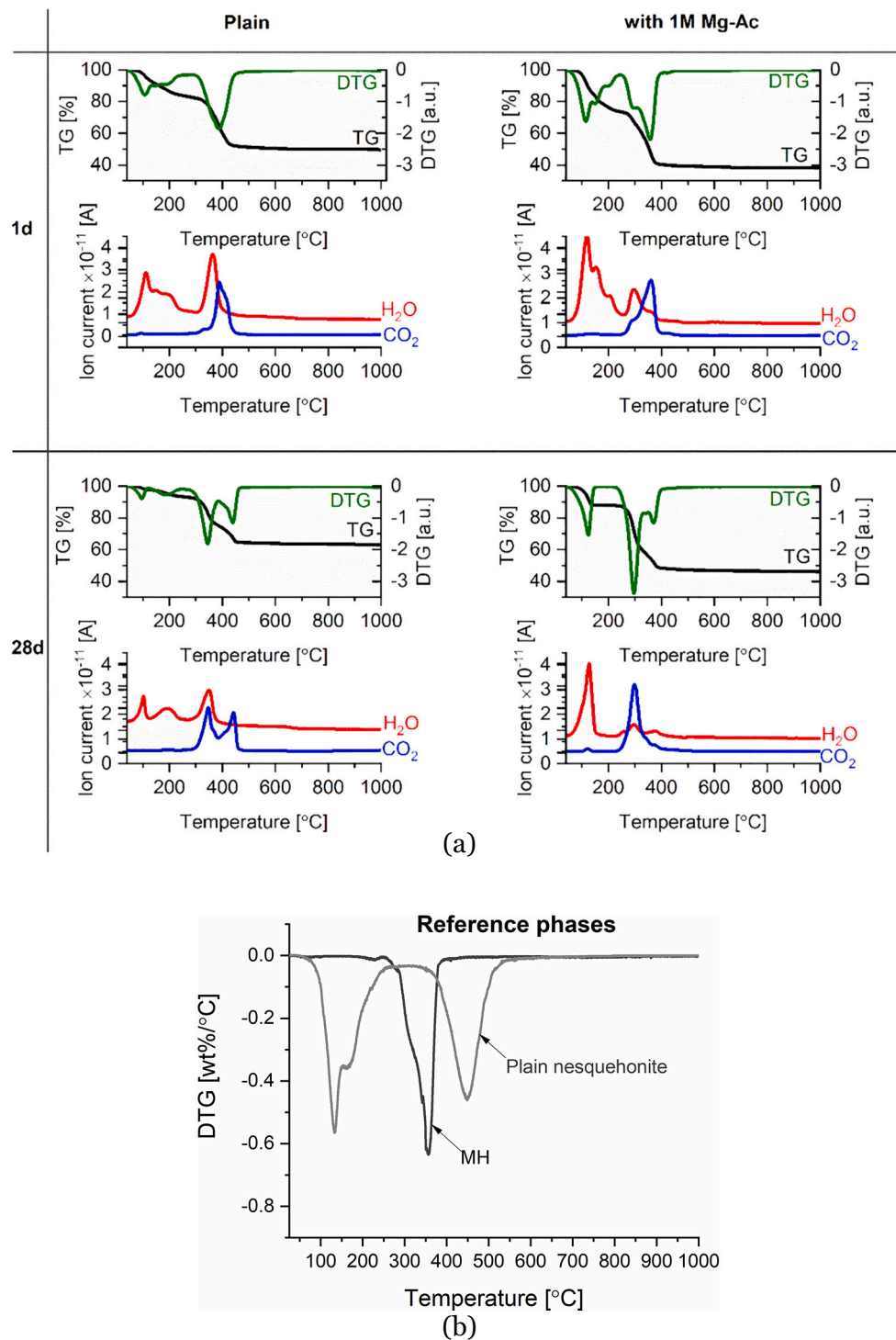


Fig. 5. TG/MS analyses of the precipitates of carbonated brucite (a) without and with the presence of 1 M Mg-Ac and (b) pure brucite and nesquehonite.

brucite returned identical to those dissolved in water. This is in good agreement with what we observed in thermal analysis of the solids (Fig. 9) and the trend of Mg concentration in solutions (Fig. A1), proving the sorption-desorption of acetate ligand on brucite.

4. Discussion

4.1. The precipitation of HMCs and kinetics of brucite carbonation

In the plain sample, nesquehonite formed as a primary precipitate

since the phase is kinetically favorable possibly due to its simple crystal structure. However, nesquehonite is a metastable phase and hence converted quickly to dypingite as seen in XRD and SEM data (Fig. 1 and Fig. 6). The conversion of this phase was captured previously [35,46] in which dypingite and dypingite-like phases precipitated on nesquehonite's surface. We observed similar phenomenon via SEM images as well as TEM analyses (see Fig. A2). Notably, HCO_3^- plays an important role in the system since the anion acts as a catalyst to promote the dissolution of brucite [49]. This is due to the formation of multidentate mono-nuclear surface complexes between CO_3^{2-} and Mg^{2+} , which destabilized

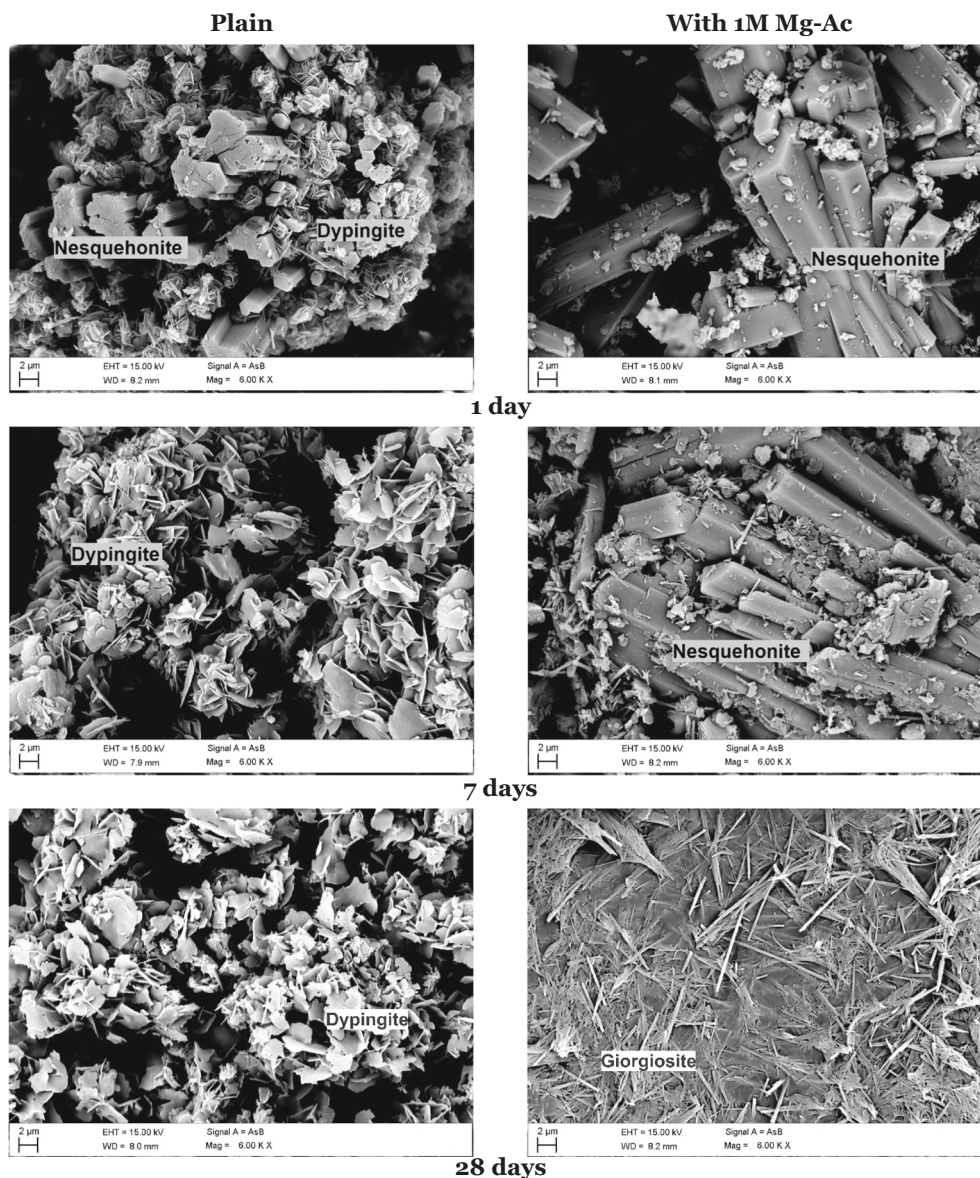


Fig. 6. Morphology of the precipitates of carbonated brucite without and with 1 M Mg-Ac.

Mg—O bonds in brucite. However, the dissolution of brucite is a surface-controlled process in a wide range of pH [50,51], and at pH above 10 the bicarbonate-carbonate equilibrium tends toward increasing the fraction of carbonates. Here, the pH of the plain sample reached basic conditions, that led to a reduction of brucite dissolved and eventually attained a low degree of reaction (i.e., ca. 50% after 28 days) in this system. In addition, Hövelmann et al. [21] observed HMCs cover brucite's surface during their precipitation via atomic force microscopy; this led potentially to surface passivation of brucite and may reduce the carbonation degree.

The presence of Mg-acetate alters the kinetics of brucite's carbonation and the phases formation. The ligand retarded the precipitation of HMCs slightly as observed via the heat evolution of the suspension (Fig. 7). However, the cumulative heat release after the first day of reaction surpassed the plain sample already. This is in-line with a much higher reaction degree of brucite in the ligand-containing sample compared to the reference in the same time period (Fig. 2). Brucite reached a reaction degree of 100% after 28 days in Mg-acetate solution, meaning the presence of acetate doubled the reaction degree, while the pH was lower than the plain sample.

Regarding the mineralogy, Mg-acetate changed the formation of

HMCs in the system. Nesquehonite remained the major phase until it converted to giorgiosite after 28 days of reaction, which contrasts with the dypingite formation for the case of plain sample. Giorgiosite is a relatively unknown HMC and there is not much information about the phase in open literature. Reports in the literature are inconsistent with the amount of water molecules contained in giorgiosite (i.e., often 5 or 6 H₂O is seen) [27,52,53]. The phase is of immediate interest since its morphology is a needle-like shape with very high fiber aspect ratio (Fig. 6), which is favorable to improve the mechanical properties and toughness of the binding material. This can explain the increase in the compressive strength of Mg-based binder from reactive MgO [13,14]. The role of giorgiosite in enhancing mechanical properties will require further investigation in actual paste or mortar samples. In addition, the quantification of amorphous fraction in the sample remains challenging since there is no crystal structure of dypingite and giorgiosite available in the open literature.

Thermodynamic modelling can predict the precipitation of HMCs in the plain sample precisely. Here we used the reaction degree of brucite as kinetic input in the modelling (Fig. 12a) where an empirical equation, proposed and described in details in Ref. [54], was used to fit the

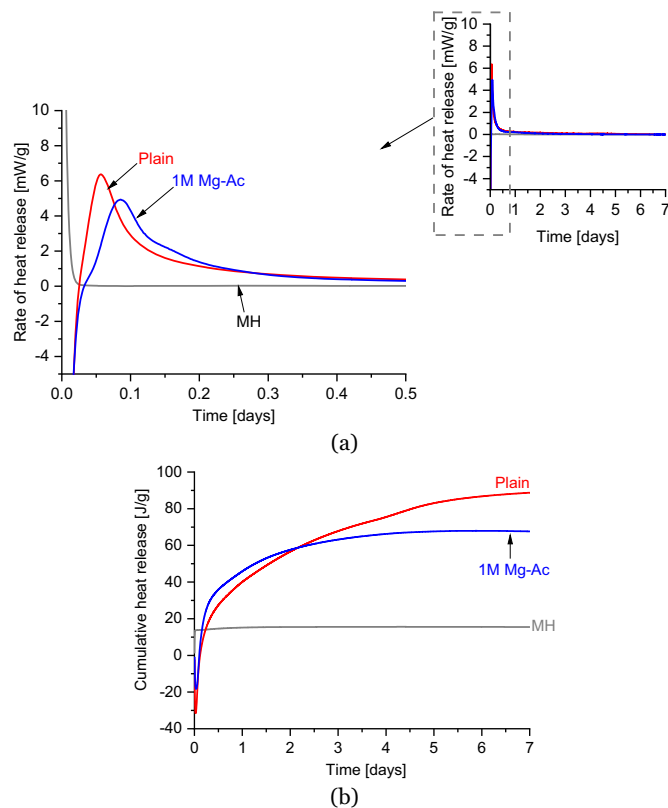


Fig. 7. The heat of carbonating brucite in aqueous environment measured by isothermal calorimetry, including (a) the rate of heat release and (b) the cumulative heat release. Note that MH (i.e., brucite in water without the presence of NaHCO_3) did not show any heat evolution since the phase did not dissolve in water and thus no exothermic reaction occurred in this sample.

experimental data. Additionally, hydromagnesite and artinite were left out of the model since both phases were not found in the experiments reported in this work. In the plain sample, the thermodynamic model could capture the formation of nesquehonite and its conversion to dypingite at later stage when more brucite reacted. This agrees with the observation via XRD shown in Fig. 1 where there was only a minor trace of dypingite detected after 1 day of reaction. From 7 days onward, dypingite remained the major precipitate besides unreacted brucite for both experiments and the thermodynamic predictions. Note that the conversion from nesquehonite to dypingite started already after 1 day (Fig. 6) and was faster than predicted in the modelling; this can be due to the fast kinetics of the conversion happened on nesquehonite's surface [35,46].

In contrast, the thermodynamic database for HMC species requires further details of missing and unavailable phases for better prediction for precipitates in this system. In ligand-containing samples, there was a mismatch between experimental data and thermodynamic modelling. Instead of dypingite, giorgiosite was found as the main HMC after the conversion from nesquehonite in 1 M Mg-Ac solution (Fig. 1). Based on the stoichiometry of giorgiosite, we estimated its thermodynamic data to be similar to dypingite. However, with this input, the thermodynamic model suggested that giorgiosite and dypingite could not co-existing, which also requires a thorough experimental investigation. This shows that the relation between these phases needs to be determined in greater detail for the thermodynamic properties of giorgiosite as well as other missing HMCs (Table 2); which is outside of the scope of this work but will improve the capability of thermodynamic modelling for the HMC-based binders in future studies. However, the approach to model the acetate ligand appears promising for the modelling of organic ligands and their complexation. Acetate was predicted to stay in the aqueous

solution as free anions or complexes with Na^+ . This explained the lower pH in the ligand-containing sample compared to that of plain sample as shown in Fig. 3. Furthermore, the presence of Mg-acetate supplied more Mg^{2+} to form HMCs leading to higher amount of HMCs precipitating compared to the reference.

4.2. The role of Mg-acetate and its interaction with hydrated magnesium carbonates

Based on the experimental results, there was a synergistic effect between Mg-acetate and HCO_3^- to promote the dissolution of brucite that enhanced the degree of reaction of brucite. First, bicarbonate undergoes a proton-transfer reaction, generating electrophilic centers (H^+) for the subsequent electrophilic substitution reaction with brucite (Eqs. (2) and (3))



and



In the plain sample, the reaction products of these reactions $\text{Mg}^{2+}(\text{aq})$ and CO_3^{2-} enrich close to the brucite surface, quickly reach supersaturation, and precipitate as nesquehonite may block sterically further reaction. The phase then converted to dypingite when there was more OH^- available in the suspension.

In contrast, in the presence of Mg-acetate, Mg^{2+} is readily available in the system in the form of free cations and Mg-acetate aqueous complexes $[\text{Mg}(\text{Acetate})^+(\text{aq})]$ and $[\text{Mg}(\text{Acetate})_2(\text{aq})]$ as listed in Table 4. The carbonate ions in excess from reactions 1 and 2 would react with the Mg^{2+} -acetate complexes via electrostatic interactions, causing the decrease in the stability of these complexes (Fig. 13); similarly than what has been observed for Mg-urea complexes previously [55,56]. Consequently, the bonds between Mg^{2+} and CH_3COO^- weakened gradually and the counterpart between Mg^{2+} and O^{2-} (in CO_3^{2-}) formed instead. Once the bonds between Mg^{2+} and acetate were destroyed and the bonds between Mg^{2+} and CO_3^{2-} established, this became an active initial nucleation site for the growth of HMCs (in this case nesquehonite). The nucleation sites act as a sink for Mg^{2+} to grow nesquehonite pushing the brucite to dissolve toward the right-hand side of Eq. (3), and since the acetate ions compete for the $\text{Mg}^{2+}(\text{aq})$ against CO_3^{2-} , precipitation occurs further away from the surface, keeping the brucite's surface open for further dissolution. The effects of nucleation sites were particularly clear in the case of highest Mg-acetate concentration (i.e., 1 M) as observed experimentally. Mg^{2+} and carbonates in the solution may formed HMC precipitate which might also act as nucleation sites. Furthermore, once nucleated the HMC precipitation rates are further increased with the increasing of acetate concentration in the solutions, and the rate of crystal growth in general is a monotonic function of the supersaturation levels [57]. This is also plausible explanation for much higher degree of reaction of brucite in Mg-acetate solution in comparison to water.

Acetate ligand is known to have little effectiveness on increasing the dissolution of brucite [49]. This is because acetate forms monodentate surface complexes on Mg—O bonds in brucite, hence promote brucite's dissolution to a lesser extent than other chelating agents (e.g., EDTA) that form surface chelates [49]. From a thermodynamic point of view, the complexation between acetate and Mg^{2+} as well as Na^+ is weak (Table 4). Note that Pokrovsky et al. [49] investigated the effects of acetate on the dissolution of brucite at much lower ionic strength (i.e., 0.3 M) than this present work. Hence, high concentration of acetate potentially leads to higher sorption of ligand on brucite's surface. This caused more predominant formation of etch pits (Fig. 10) in the ligand-containing solution and eventually increased the dissolution of brucite. Furthermore, the sorption and desorption of the ligand on brucite's surface seems to be predominant at high concentration of Mg-acetate

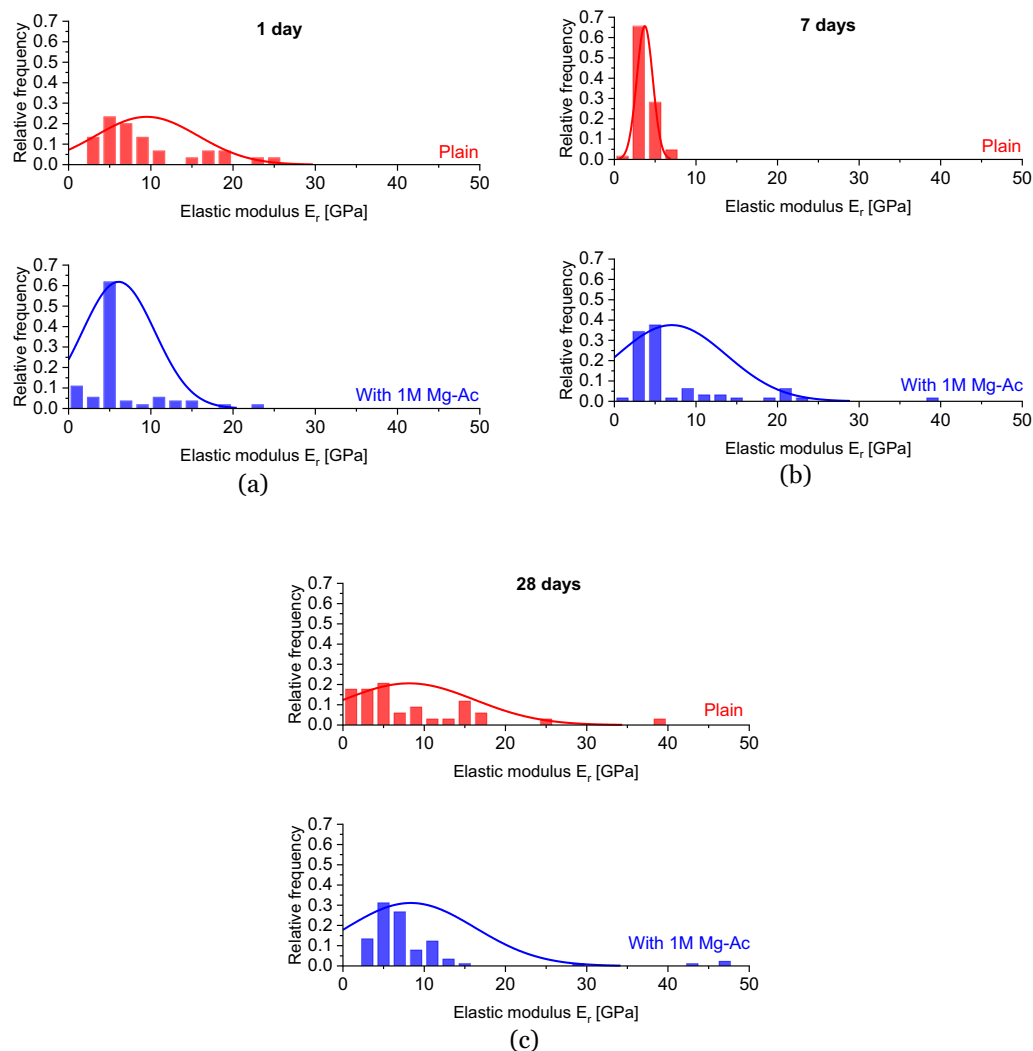


Fig. 8. The elastic modulus of precipitates with and without the presence of Mg—Ac after (a) 1, (b) 7, and (c) 28 days.

(Fig. 9–Fig. 11). Since the structure of brucite consists of MgO_6 octahedra sheets stacked in layers [58], the peeled-off morphology of brucite after the dissolution in Mg-acetate solution (Fig. 10) reveals the sorption of acetate ligand between layers in the mineral likely facilitated by a structural weakness among these layers. Notably, the pH of the system plays an important role letting ligands act as catalysts or inhibitors [59,60]. In neutral or weak alkaline solution, acetate has limited effect on the increase of the dissolution of brucite; however, at $\text{pH} > 10.5$, the ligand turns into an inhibitor [49].

The interaction between acetate ligand and HMCs may provide important insights into the stability of HMCs and requires further investigations. The ligand altered the morphology of nesquehonite (Fig. 6) and the route for nesquehonite to convert to giorgiosite instead of dypingite in the case of the plain sample. Although both giorgiosite and dypingite have similar (even the same) chemical formula [61], the morphology and crystal structure are distinguishable. Interestingly, Jia et al. [56] observed the formation of dypingite in the form of nanowires, which are completely different from the flakey form of this phase. In addition, the conversion from nesquehonite to giorgiosite happened with much slower kinetics than that of dypingite. Therefore, the ligand potentially increased the stability of giorgiosite and/or solubility of dypingite. However, there is a remaining open question whether giorgiosite will convert to other HMCs over time. In the plain sample, dypingite seems convert to hydromagnesite as the phase is an intermediate hydrate between nesquehonite and hydromagnesite [35]. This is

particularly important for the durability aspect of these cementitious materials which may affect the mechanical performance of construction materials in the long term.

4.3. Mechanical properties of the precipitates

The presence of Mg-acetate increased the elastic modulus of the phases formed (Fig. 8). The contribution of the ligand was more profound for longer hydration times, while there were no significant effects on the elastic modulus after 1 day. This can be attributed to the altering in the phase assemblage of HMCs in the ligand-containing sample compared with the reference (see Fig. 1 and Fig. 6). In contrast, the plain sample showed a relatively stable range of elastic modulus except for the sample after 7 days. This can be due to the conversion among different metastable HMCs as discussed previously (Section 4.1). Dung et al. [16] reported the average elastic moduli of brucite and HMCs to be ca. 2.5 and 19.4 GPa, respectively. Our experimental data show good agreement with the previously reported values in the literature [16], although the modulus range can be different among HMCs. In addition, similarly to other works [16,62], there was a challenge to distinguish and allocate the contribution of different HMCs in various ranges of modulus. To this end and prior to the deconvolution of distribution from nano indentation, there is a need for more dedicated investigation with a larger number of data points for a proper statistic and a characterizing technique to measure the elastic modulus of pure HMCs especially for

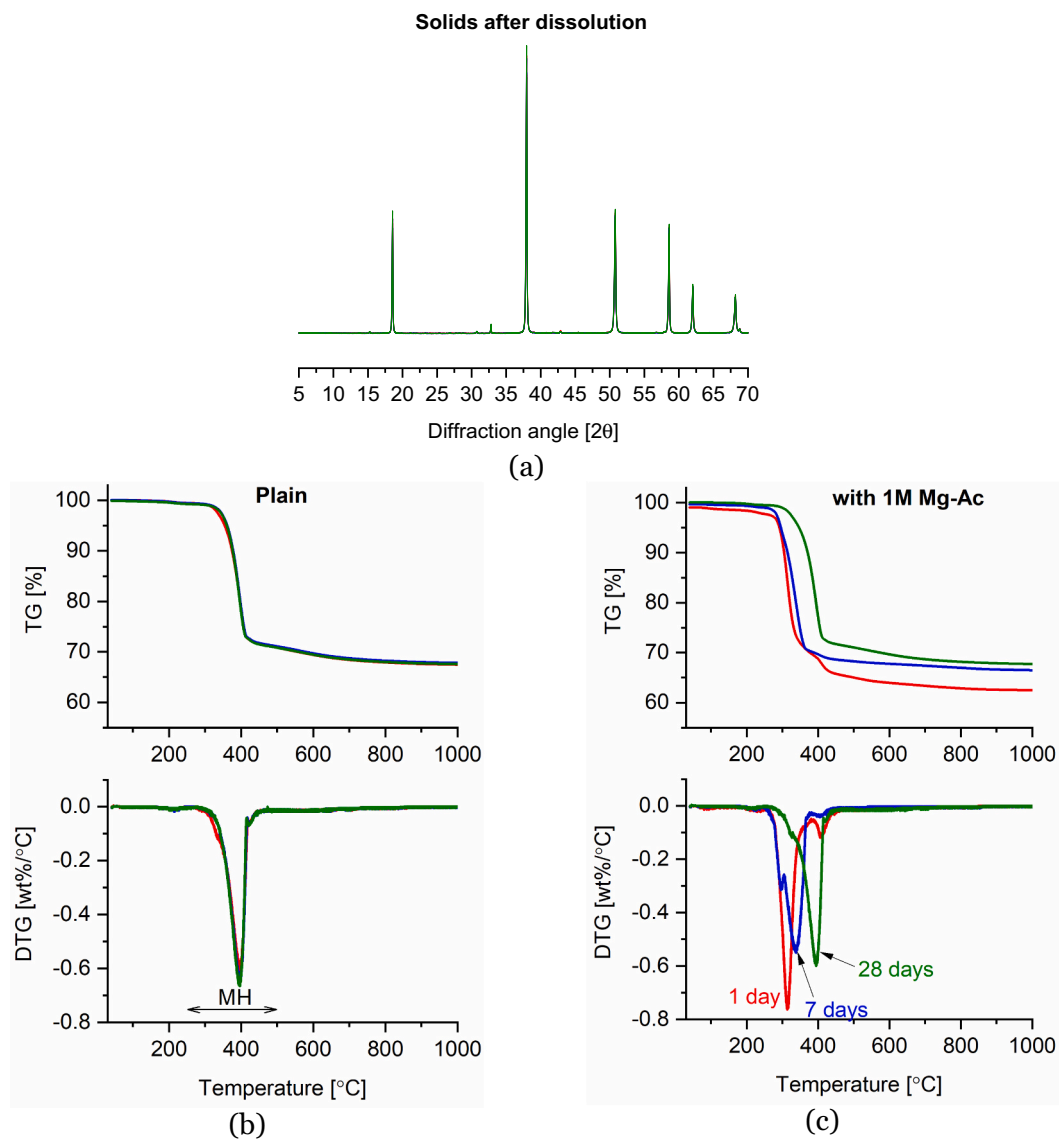


Fig. 9. (a) The XRD diffractograms of all solid samples in both water and Mg—Ac solution, and TG/DTG analyses of the brucite after dissolution tests in (b) water and (c) 1 M Mg-Ac solution after 1–28 days.

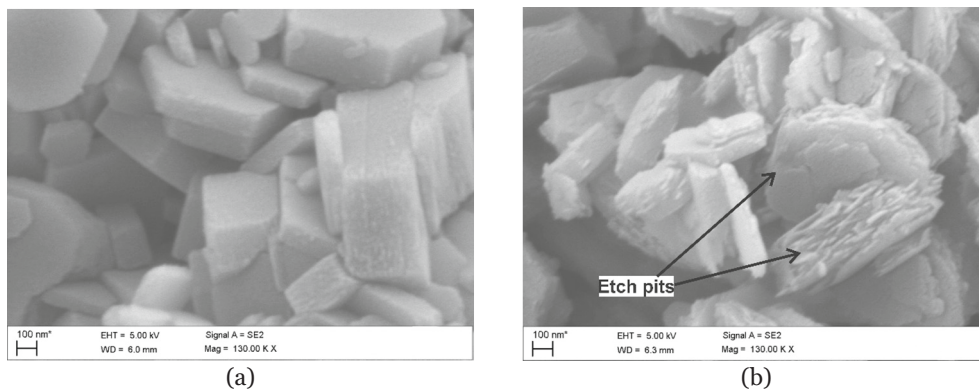


Fig. 10. Morphology of brucite after the dissolution in (a) water and (b) 1 M Mg-Ac solution.

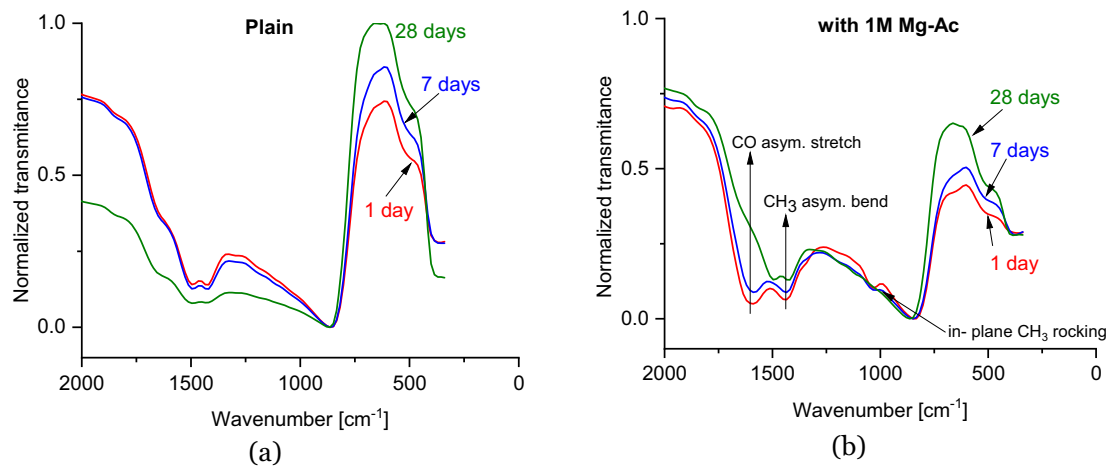


Fig. 11. FTIR spectra of the brucite after the dissolution test in (a) water and (b) in 1 M Mg-Ac solution after 1–28 days.

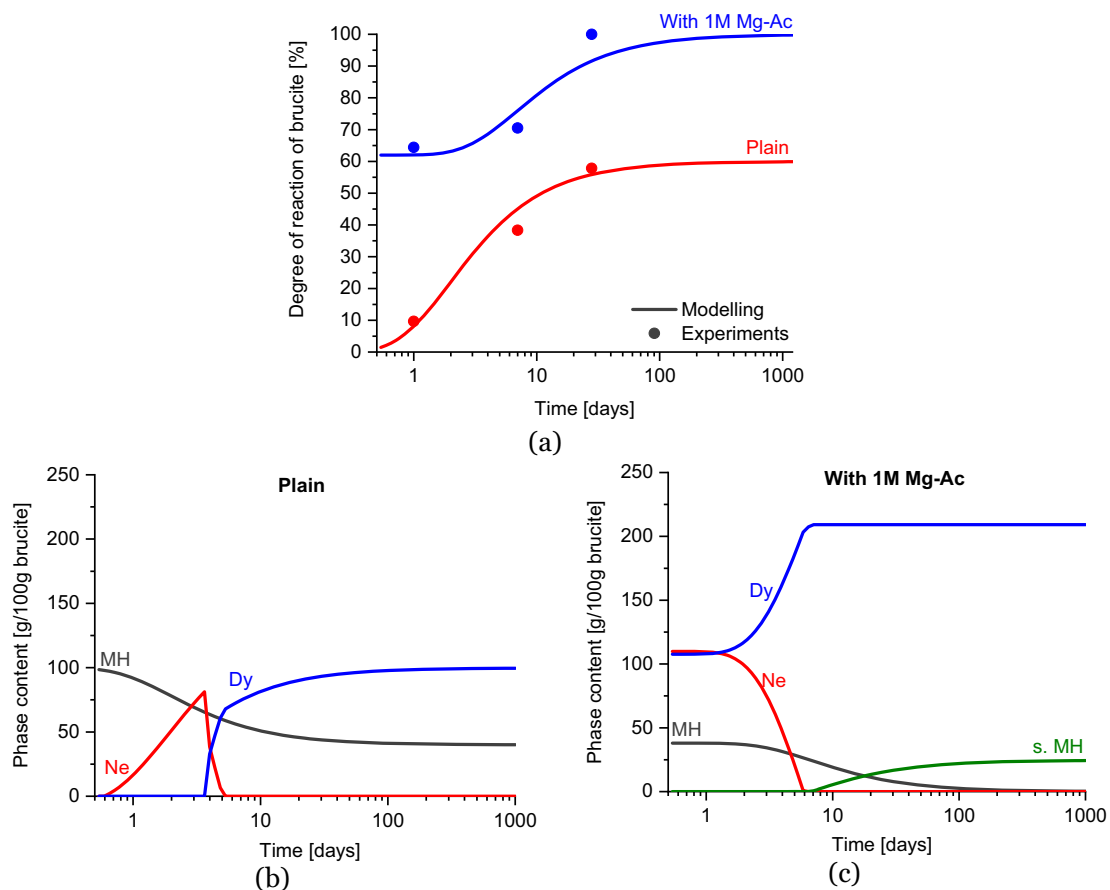


Fig. 12. (a) The kinetics input for thermodynamic modelling based on the reaction degree of brucite and the predicted precipitates in (b) water and (c) 1 M Mg-Ac solution. Note that Dy = dypingite, Ne = nesquehonite, MH = brucite, and s. MH = secondary brucite.

unknown phase such as giorgiosite.

5. Conclusions

The present work reports the effects of Mg-acetate on the carbonation of brucite in aqueous environment. Brucite is an important intermediate phase prior to its carbonation to form HMCs in MgO-based binders. Here, we addressed several open research questions: the role of acetate ligand on the carbonation of brucite, the kinetics of reaction, and

the formation of different HMCs.

Nesquehonite forms with fast kinetics due to its simple crystal structure. However, the phase is metastable and converts quickly to dypingite. The presence of acetate ligand increases the kinetics and reaction degree of brucite's carbonation. Nesquehonite converts with a low rate to giorgiosite in ligand-containing sample. Giorgiosite is a relatively unknown HMC and there is a need for more understanding about the crystal (e.g., thermodynamic properties and crystal structure). The differences in phase assemblage between the plain and ligand-

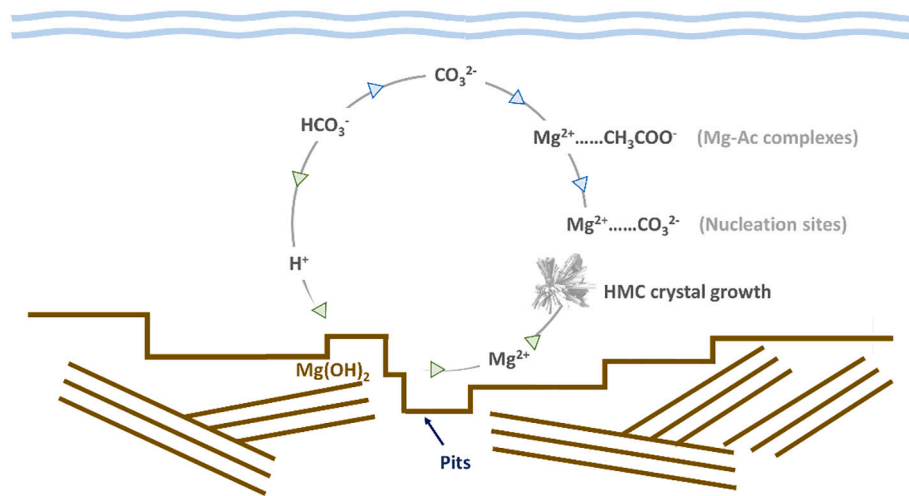


Fig. 13. A schematic reaction pathway of brucite in aqueous environment with the presence of Mg–Ac.

containing samples also affect their mechanical properties. The presence of Mg-acetate increases the elastic modulus the HMCs linking to the formation of giorgiosite.

The higher reaction degree of brucite in the presence of Mg-acetate is attributed to the formation nucleation sites in the solution. The bonds between Mg^{2+} and CO_3^{2-} establish after breaking the complexes between Mg^{2+} and acetate ligand. Consequently, this becomes active initial nucleation sites for the growth of HMCs. The nucleation sites act as a sink for Mg^{2+} to grow HMCs and prevent the formation of passivation layer on brucite's surface. We also found the sorption and desorption of the acetate ligand on brucite at high concentration of Mg-acetate.

Further investigation on the properties of giorgiosite as well as other unknown HMCs are necessary toward better prediction and understanding of the relationship among HMCs. The interaction between organic ligands and HMCs is of increasing interest since this will be a key information to explain why acetate led to the formation of giorgiosite instead of dypingite.

CRedit authorship contribution statement

Hoang Nguyen: Conceptualization, Data curation, Formal analysis, Investigation, Methodology, Validation, Visualization, Writing – original draft, Writing – review & editing. **Hellen Santos:** Investigation, Methodology, Validation, Visualization, Writing – review & editing.

Appendix A

Harisankar Sreenivasan: Data curation, Investigation, Methodology. **Wolfgang Kunther:** Methodology, Data curation, Formal analysis, Writing – review & editing. **Valter Carvelli:** Methodology, Data curation, Formal analysis, Writing – review & editing. **Mirja Illikainen:** Resources, Writing – review & editing, Funding acquisition. **Paivo Kinnunen:** Conceptualization, Formal analysis, Validation, Resources, Supervision, Writing – review & editing, Funding acquisition.

Declaration of competing interest

The authors declare that they have no known competing financial interests or personal relationships that could have appeared to influence the work reported in this paper.

Acknowledgement

P.K. and H.N. are grateful for the financial support from the University of Oulu & The Academy of Finland Profi5 326291, as well as the Academy of Finland project 329477. The authors thank Viljami Viinikka, Durgaprasad Ramteke, Jarno Karvonen, Tommi Kokkonen, Heini Tuorila, and Ebba Schnell for the support during the work. A part of the material characterization was carried out with the support from the Centre for Material Analysis, University of Oulu, Finland. We thank the interdisciplinary 'In-Situ Micromechanics Laboratory' of Politecnico di Milano for the nanoindentation equipment.

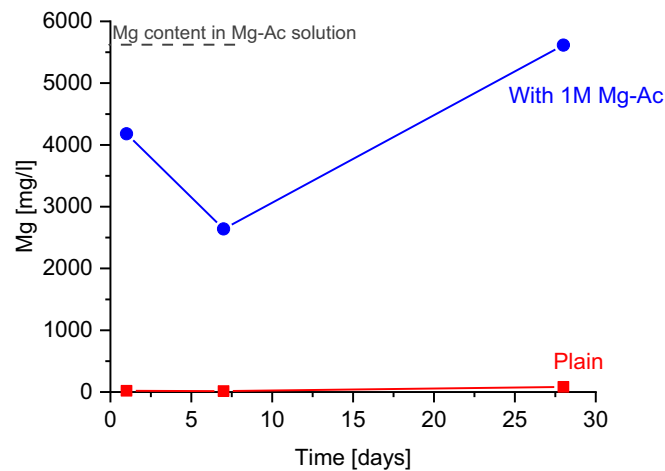


Fig. A1. The concentration of Mg at different dissolution times (1–28 days) with and without the presence of Mg—Ac measured by ICP-OES.

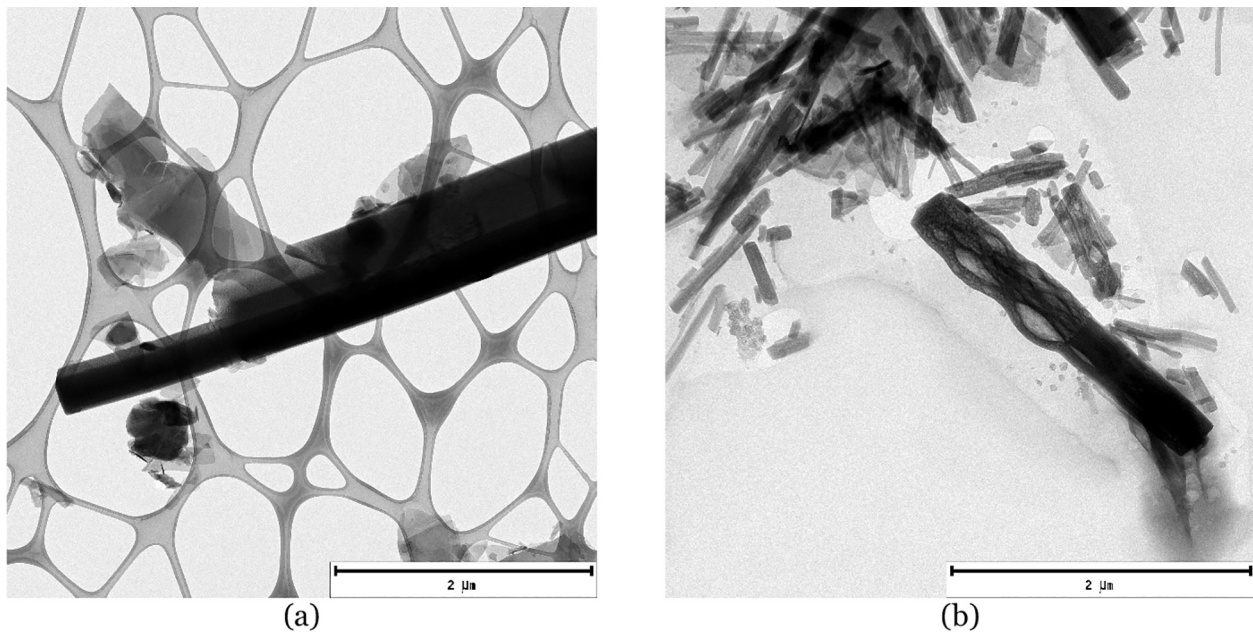


Fig. A2. The capture of conversion from (a) nesquehonite to dypingite in the plain material and (b) nesquehonite to giorgiosite in ligand-containing sample from 1 M Mg-Ac solution. The images were taken via scanning transmission electron microscope with a JEOL JEM-2200FS equipped with energy-dispersive X-ray spectroscopy (EDS) detector (JEOL Dry SD100GV, 100 mm2, 0.98 Sr).

References

- [1] World Business Council for Sustainable Development (WBCSD) Cement, Sustainability Initiative (CSI), Cement industry energy and CO2 performance—Getting the Numbers Right (GNR). http://wbcsdservers.org/wbcsdpublications/cd_files/datas/business-solutions/cement/pdf/CementIndustryEnergyAnd%20CO2Performance.pdf, 2009.
- [2] K.L. Scrivener, V.M. John, E.M. Gartner, Eco-efficient cements: potential economically viable solutions for a low-CO2 cement-based materials industry, *Cem. Concr. Res.* 114 (2018) 2–26, <https://doi.org/10.1016/j.cemconres.2018.03.015>.
- [3] R.M. Andrew, Global CO2 emissions from cement production, *Earth Syst. Sci. Data* 10 (2018) 195–217, <https://doi.org/10.5281/zenodo.831455>.
- [4] I. WBCSD, Cement Technology Roadmap 2009: carbon emissions reductions up to 2050, *World Bus. Counc. Sustain. Dev. Int. Energy Agency*, 2009.
- [5] J.W. Bullard, H.M. Jennings, R.A. Livingston, A. Nonat, G.W. Scherer, J. S. Schweitzer, K.L. Scrivener, J.J. Thomas, Mechanisms of cement hydration, *Cem. Concr. Res.* 41 (2011) 1208–1223, <https://doi.org/10.1016/j.cemconres.2010.09.011>.
- [6] M.C.G. Juenger, F. Winnefeld, J.L. Provis, J.H. Ideker, Advances in alternative cementitious binders, in: *Conf. Spec. Cem. Hydration Kinet. Model. Quebec City 2009 CONMOD10 Lausanne 2010 41, 2011*, pp. 1232–1243, <https://doi.org/10.1016/j.cemconres.2010.11.012>.
- [7] E. Gartner, T. Sui, Alternative cement clinkers, *Cem. Concr. Res.* 114 (2018) 27–39, <https://doi.org/10.1016/j.cemconres.2017.02.002>.
- [8] S. Ruan, C. Unluer, Comparative life cycle assessment of reactive MgO and Portland cement production, *J. Clean. Prod.* 137 (2016) 258–273, <https://doi.org/10.1016/j.jclepro.2016.07.071>.
- [9] R. Zevenhoven, M. Slotte, E. Koivisto, R. Erlund, Serpentine carbonation process routes using ammonium sulfate and integration in industry, *Energy Technol.* 5 (2017) 945–954, <https://doi.org/10.1002/ente.201600702>.
- [10] T. Zhang, L.J. Vandeperre, C.R. Cheeseman, Formation of magnesium silicate hydrate (M-S-H) cement pastes using sodium hexametaphosphate, *Cem. Concr. Res.* 65 (2014) 8–14, <https://doi.org/10.1016/j.cemconres.2014.07.001>.
- [11] T. Zhang, C.R. Cheeseman, L.J. Vandeperre, Development of low pH cement systems forming magnesium silicate hydrate (M-S-H), *Cem. Concr. Res.* 41 (2011) 439–442, <https://doi.org/10.1016/j.cemconres.2011.01.016>.
- [12] E. Bernard, B. Lothenbach, C. Cau-Dit-Coumes, I. Pochard, D. Rentsch, Aluminum incorporation into magnesium silicate hydrate (M-S-H), *Cem. Concr. Res.* 128 (2020), 105931, <https://doi.org/10.1016/j.cemconres.2019.105931>.
- [13] N.T. Dung, C. Unluer, Sequestration of CO2 in reactive MgO cement-based mixes with enhanced hydration mechanisms, *Constr. Build. Mater.* 143 (2017) 71–82, <https://doi.org/10.1016/j.conbuildmat.2017.03.038>.
- [14] N.T. Dung, C. Unluer, Development of MgO concrete with enhanced hydration and carbonation mechanisms, *Cem. Concr. Res.* 103 (2018) 160–169, <https://doi.org/10.1016/j.cemconres.2017.10.011>.

- [15] N.T. Dung, C. Unluer, Performance of reactive MgO concrete under increased CO₂ dissolution, *Cem. Concr. Res.* 118 (2019) 92–101, <https://doi.org/10.1016/j.cemconres.2019.02.007>.
- [16] N.T. Dung, A. Lesimple, R. Hay, K. Celik, C. Unluer, Formation of carbonate phases and their effect on the performance of reactive MgO cement formulations, *Cem. Concr. Res.* 125 (2019), 105894, <https://doi.org/10.1016/j.cemconres.2019.105894>.
- [17] C. Kuenzel, F. Zhang, V. Ferrándiz-Mas, C.R. Cheeseman, E.M. Gartner, The mechanism of hydration of MgO-hydromagnesite blends, *Cem. Concr. Res.* 103 (2018) 123–129, <https://doi.org/10.1016/j.cemconres.2017.10.003>.
- [18] F. Winnefeld, E. Epifania, F. Montagnaro, E.M. Gartner, Further studies of the hydration of MgO-hydromagnesite blends, *Cem. Concr. Res.* 126 (2019), 105912, <https://doi.org/10.1016/j.cemconres.2019.105912>.
- [19] N.T. Dung, C. Unluer, Carbonated MgO concrete with improved performance: the influence of temperature and hydration agent on hydration, carbonation and strength gain, *Cem. Concr. Compos.* 82 (2017) 152–164, <https://doi.org/10.1016/j.cemconcomp.2017.06.006>.
- [20] L. Zhao, L. Sang, J. Chen, J. Ji, H.H. Teng, Aqueous carbonation of natural brucite: relevance to CO₂ sequestration, *Environ. Sci. Technol.* 44 (2010) 406–411, <https://doi.org/10.1021/es9017656>.
- [21] J. Hövelmann, C.V. Putnis, E. Ruiz-Agudo, H. Austrheim, Direct nanoscale observations of CO₂ sequestration during brucite [Mg(OH)₂] dissolution, *Environ. Sci. Technol.* 46 (2012) 5253–5260, <https://doi.org/10.1021/es300403n>.
- [22] A.L. Harrison, I.M. Power, G.M. Dipple, Accelerated carbonation of brucite in mine tailings for carbon sequestration, *Environ. Sci. Technol.* 47 (2013) 126–134, <https://doi.org/10.1021/es3012854>.
- [23] H.T. Schaefer, C.F. Windisch, B.P. McGrail, P.F. Martin, K.M. Rosso, Brucite [Mg(OH)₂] carbonation in wet supercritical CO₂: an in situ high pressure X-ray diffraction study, *Geochim. Cosmochim. Acta* 75 (2011) 7458–7471, <https://doi.org/10.1016/j.gca.2011.09.029>.
- [24] D.A. Kulik, T. Wagner, S.V. Dmytrieva, G. Kosakowski, F.F. Hingerl, K. V. Chudnenko, U.R. Berner, GEM-selektor geochemical modeling package: revised algorithm and GEMS3K numerical kernel for coupled simulation codes, *Comput. Geosci.* 17 (2013) 1–24, <https://doi.org/10.1007/s10596-012-9310-6>.
- [25] GEM Software Main Page, (n.d.). <http://gems.web.psi.ch/> (accessed November 19, 2019).
- [26] B. Løthenbach, D.A. Kulik, T. Matschei, M. Balonis, L. Baquerizo, B. Dilnesa, G. D. Miron, R.J. Myers, Cemdata18: a chemical thermodynamic database for hydrated Portland cements and alkali-activated materials, *Cem. Concr. Res.* 115 (2019) 472–506, <https://doi.org/10.1016/j.cemconres.2018.04.018>.
- [27] G. Raade, Dypingite, a new hydrous basic carbonate of magnesium, from Norway, *Am. Miner.* 55 (1970) 1457–1465.
- [28] A.L. Harrison, V. Mavromatis, E.H. Oelkers, P. Bénéth, Solubility of the hydrated mg-carbonates nesquehonite and dypingite from 5 to 35 °C: implications for CO₂ storage and the relative stability of mg-carbonates, *Chem. Geol.* 504 (2019) 123–135, <https://doi.org/10.1016/j.chemgeo.2018.11.003>.
- [29] E. Königsberger, L.-C. Königsberger, H. Gamsjäger, Low-temperature thermodynamic model for the system Na₂CO₃–MgCO₃–CaCO₃–H₂O, *Geochim. Cosmochim. Acta* 63 (1999) 3105–3119, [https://doi.org/10.1016/S0016-7037\(99\)00238-0](https://doi.org/10.1016/S0016-7037(99)00238-0).
- [30] R.J. Hill, J.H. Canterford, F.J. Moyle, New data for lansfordite, *Mineral. Mag.* 46 (1982) 453–457, <https://doi.org/10.1180/minmag.1982.046.341.08>.
- [31] Q. Gautier, P. Bénéth, V. Mavromatis, J. Schott, Hydromagnesite solubility product and growth kinetics in aqueous solution from 25 to 75 °C, *Geochim. Cosmochim. Acta* 138 (2014) 1–20, <https://doi.org/10.1016/j.gca.2014.03.044>.
- [32] R.A. Robie, B.S. Hemingway, The heat capacities at low-temperatures and entropies at 298.15 K of nesquehonite, MgCO₃·3H₂O, and hydromagnesite, *Am. Miner.* 57 (1972) 1768–1781.
- [33] W. Hummel, U. Berner, E. Curti, F.J. Pearson, T. Thoenen, Nagra/PSI chemical thermodynamic data base 01/01, *Radiochim. Acta* 90 (2002) 805–813, <https://doi.org/10.1524/ract.2002.90.9-11.2002.805>.
- [34] H.C. Helgeson, J.M. Delany, H.W. Nesbitt, D.K. Bird, Summary and critique of the thermodynamic properties of rock-forming minerals, *Am. J. Sci.* 278A (n.d.) 1–299.
- [35] L. Hopkinson, P. Kristova, K. Rutt, G. Cressey, Phase transitions in the system MgO–CO₂–H₂O during CO₂ degassing of mg-bearing solutions, *Geochim. Cosmochim. Acta* 76 (2012) 1–13, <https://doi.org/10.1016/j.gca.2011.10.023>.
- [36] M. Hänchen, V. Prigobbe, R. Baciocchi, M. Mazzotti, Precipitation in the mg-carbonate system—effects of temperature and CO₂ pressure, *Chem. Eng. Sci.* 63 (2008) 1012–1028, <https://doi.org/10.1016/j.ces.2007.09.052>.
- [37] M. Wedenig, R. Boch, A. Leis, H. Wagner, M. Dietzel, Green inhibitor performance against CaCO₃ scaling: rate-modeling aided test procedure, *Cryst. Growth Des.* 21 (2021) 1959–1971, <https://doi.org/10.1021/acs.cgd.0c01258>.
- [38] R.L. Frost, J.T. Klopogge, Infrared emission spectroscopic study of brucite, *Spectrochim. Acta A Mol. Biomol. Spectrosc.* 55 (1999) 2195–2205, [https://doi.org/10.1016/S1386-1425\(99\)00016-5](https://doi.org/10.1016/S1386-1425(99)00016-5).
- [39] R.L. Frost, S.J. Palmer, Infrared and infrared emission spectroscopy of nesquehonite Mg(OH)(HCO₃)·2H₂O—implications for the formula of nesquehonite, *Spectrochim. Acta A Mol. Biomol. Spectrosc.* 78 (2011) 1255–1260, <https://doi.org/10.1016/j.saa.2010.12.059>.
- [41] V. Skliros, A. Anagnostopoulou, P. Tsakiridis, M. Perraki, Mineralogical and spectroscopic study of nesquehonite synthesized by reaction of gaseous CO₂ with mg chloride solution, *Bull. Geol. Soc. Greece* 50 (2016) 2017, <https://doi.org/10.12681/bgsg.11947>.
- [41] J.T. Klopogge, W.N. Martens, L. Nothdurft, L.V. Duong, G.E. Webb, Low temperature synthesis and characterization of nesquehonite, *J. Mater. Sci. Lett.* 22 (2003) 825–829, <https://doi.org/10.1023/A:1023916326626>.
- [42] E.E. Coleyshaw, G. Crump, W.P. Griffith, Vibrational spectra of the hydrated carbonate minerals ikaite, monohydrocalcite, lansfordite and nesquehonite, *Spectrochim. Acta A Mol. Biomol. Spectrosc.* (2003) 2231–2239, [https://doi.org/10.1016/S1386-1425\(03\)00067-2](https://doi.org/10.1016/S1386-1425(03)00067-2). Elsevier.
- [43] R.L. Frost, S. Bahfenne, J. Graham, B.J. Reddy, The structure of selected magnesium carbonate minerals - a near infrared and mid-infrared spectroscopic study, *Polyhedron* 27 (2008) 2069–2076, <https://doi.org/10.1016/j.poly.2008.03.019>.
- [44] G. Jauffret, J. Morrison, F.P. Glasser, On the thermal decomposition of nesquehonite, *J. Therm. Anal. Calorim.* 122 (2015) 601–609, <https://doi.org/10.1007/s10973-015-4756-0>.
- [45] F.P. Glasser, G. Jauffret, J. Morrison, J.-L. Galvez-Martos, N. Patterson, M.S.-E. Imbabi, Sequestering CO₂ by mineralization into useful nesquehonite-based products, *Front. Energy Res.* 4 (2016), <https://doi.org/10.3389/fenrg.2016.00003>.
- [46] K. Mitsuhashi, N. Tagami, K. Tanabe, T. Ohkubo, H. Sakai, M. Koishi, M. Abe, Synthesis of microtubes with a surface of “House of cards” structure via needlelike particles and control of their pore size, *Langmuir* 21 (2005) 3659–3663, <https://doi.org/10.1021/la047580o>.
- [47] Z. Luo, W. Li, K. Wang, S.P. Shah, Research progress in advanced nanomechanical characterization of cement-based materials, *Cem. Concr. Compos.* 94 (2018) 277–295, <https://doi.org/10.1016/j.cemconcomp.2018.09.016>.
- [48] S.-F. Pang, C.-Q. Wu, Q.-N. Zhang, Y.-H. Zhang, The structural evolution of magnesium acetate complex in aerosols by FTIR-ATR spectra, *J. Mol. Struct.* 1087 (2015) 46–50, <https://doi.org/10.1016/j.molstruc.2015.01.034>.
- [49] O.S. Pokrovsky, J. Schott, A. Castillo, Kinetics of brucite dissolution at 25 °C in the presence of organic and inorganic ligands and divalent metals, *Geochim. Cosmochim. Acta* 69 (2005) 905–918, <https://doi.org/10.1016/j.gca.2004.08.011>.
- [50] O.S. Pokrovsky, J. Schott, Experimental study of brucite dissolution and precipitation in aqueous solutions: surface speciation and chemical affinity control, *Geochim. Cosmochim. Acta* 68 (2004) 31–45, [https://doi.org/10.1016/S0016-7037\(03\)00238-2](https://doi.org/10.1016/S0016-7037(03)00238-2).
- [51] G. Jordan, W. Rammensee, Dissolution rates and activation energy for dissolution of brucite (001): a new method based on the microtopography of crystal surfaces, *Geochim. Cosmochim. Acta* 60 (1996) 5055–5062, [https://doi.org/10.1016/S0016-7037\(96\)00309-2](https://doi.org/10.1016/S0016-7037(96)00309-2).
- [52] B. Friedel, *Synthetischer giorgiosit, Neues Jahrb. Miner. Monatsh.* 1975 (1975) 196–208.
- [53] J. Suzuki, M. Ito, A new magnesium carbonate hydrate mineral, Mg₅(CO₃)₄(OH)·2H₂O, from Yoshikawa, Aichi Prefecture, Japan, *J. Jpn. Assoc. Mineral. Econ. Geol.* 68 (1973) 353–361, <https://doi.org/10.2465/GANKO1941.68.353>.
- [54] W. Kunther, Z. Dai, J. Skibsted, Thermodynamic modeling of hydrated white Portland cement–metakaolin–limestone blends utilizing hydration kinetics from 29Si MAS NMR spectroscopy, *Cem. Concr. Res.* 86 (2016) 29–41, <https://doi.org/10.1016/j.cemconres.2016.04.012>.
- [55] C. Yan, D. Xue, Novel self-assembled MgO nanosheet and its precursors, *J. Phys. Chem. B* 109 (2005) 12358–12361, <https://doi.org/10.1021/jp050644z>.
- [56] Y. Jia, T. Luo, X.-Y. Yu, B. Sun, J.-H. Liu, X.-J. Huang, A facile template free solution approach for the synthesis of dypingite nanowires and subsequent decomposition to nanoporous MgO nanowires with excellent arsenate adsorption properties, *RSC Adv.* 3 (2013) 5430–5437, <https://doi.org/10.1039/C3RA23340E>.
- [57] F.K. Crundwell, Concerning the influence of surface charge on the rate of growth of surfaces during crystallization, *Cryst. Growth Des.* 16 (2016) 5877–5886, <https://doi.org/10.1021/acs.cgd.6b00939>.
- [58] J.F.W. Bowles, Hydroxides, in: D. Alderton, S.A. Elias (Eds.), *Encycl. Geol.*, Second Ed., Academic Press, Oxford, 2021, pp. 442–451, <https://doi.org/10.1016/B978-0-08-102908-4.00162-4>.
- [59] S.V. Golubev, A. Bauer, O.S. Pokrovsky, Effect of pH and organic ligands on the kinetics of smectite dissolution at 25 °C, *Geochim. Cosmochim. Acta* 70 (2006) 4436–4451, <https://doi.org/10.1016/j.gca.2006.06.1557>.
- [60] S.P. Veetil, A. Mucci, T. Arakaki, Dolomite dissolution kinetics in aqueous solutions in the presence of organic and inorganic additives at 25 °C and pCO₂ ~ 1 atm, *Chem. Geol.* 483 (2018) 98–110, <https://doi.org/10.1016/j.chemgeo.2018.02.025>.
- [61] M. Liska, A. Wilson, J. Bensted, 13 - special cements, in: P.C. Hewlett, M. Liska (Eds.), *Leas Chem. Cem. Concr. Fifth Ed.*, Butterworth-Heinemann, 2019, pp. 585–640, <https://doi.org/10.1016/B978-0-08-100773-0.00013-7>.
- [62] N.T. Dung, R. Hay, A. Lesimple, K. Celik, C. Unluer, Influence of CO₂ concentration on the performance of MgO cement mixes, *Cem. Concr. Compos.* 115 (2021), 103826, <https://doi.org/10.1016/j.cemconcomp.2020.103826>.